On the selection of AGN neutrino source candidates for a source stacking analysis with neutrino telescopes

A. Achterberg [y], M. Ackermann [aa], J. Adams [h], J. Ahrens [p], D. W. Atlee [w], J. N. Bahcall [s,1], X. Bai [r], B. Baret [f], M. Bartelt [j], S. W. Barwick [k], R. Bay [c], K. Beattie [d], T. Becka [p], J. K. Becker [j], K.-H. Becker [z], P. Berghaus [e], D. Berley [i], E. Bernardini [aa], D. Bertrand [e], D. Z. Besson [ℓ], E. Blaufuss [i], D. J. Boersma [o], C. Bohm [u], S. Böser [aa], O. Botner [x], A. Bouchta [x], J. Braun [o], C. Burgess [u], T. Burgess [u], T. Castermans [q], D. Chirkin [d], J. Clem [r], B. Collin [w], J. Conrad [x], J. Cooley [o], D. F. Cowen [w,v], M. V. D'Agostino [c], A. Davour [x], C. T. Day [d], C. De Clercq [f], P. Desiati [o], T. DeYoung [w], J. Dreyer [j], M. R. Duvoort [y], W. R. Edwards [d], R. Ehrlich [i], R. W. Ellsworth [i], P. A. Evenson [r], A. R. Fazely [b], T. Feser [p], K. Filimonov [c], T. K. Gaisser [r], J. Gallagher [n], R. Ganugapati [o], H. Geenen [z], L. Gerhardt [k], A. Goldschmidt [d], J. A. Goodman [i], M. G. Greene [w], S. Grullon [o], A. Groß [j,*], R. M. Gunasingha [b], A. Hallgren [x], F. Halzen [o], K. Han [h], K. Hanson [o], D. Hardtke [c], R. Hardtke [t], T. Harenberg [z], J. E. Hart [w], T. Hauschildt [r], D. Hays [d], J. Heise [y], K. Helbing [d], M. Hellwig [p], P. Herquet [q], G. C. Hill [o], J. Hodges [o], K. D. Hoffman [i], K. Hoshina [o], D. Hubert [f], B. Hughey [o], P. O. Hulth [u], K. Hultqvist [u], S. Hundertmark [u], A. Ishihara [o], J. Jacobsen [d], G. S. Japaridze [a], A. Jones [d], J. M. Joseph [d], K.-H. Kampert [z], A. Karle [o], H. Kawai [g], J. L. Kelley [o], M. Kestel [w], N. Kitamura [o], S. R. Klein [d], S. Klepser [aa], G. Kohnen [q], H. Kolanoski [aa,2], L. Köpke [p], M. Krasberg [o], K. Kuehn [k], H. Landsman [o], R. Lang [aa], H. Leich [aa], M. Leuthold [aa], I. Liubarsky [m], J. Lundberg [x], J. Madsen [t], K. Mase [g], H. S. Matis [d], T. McCauley [d], C. P. McParland [d], A. Meli [j], T. Messarius [j], P. Mészáros [w,v], R. H. Minor [d],

P. Miočinović [c], H. Miyamoto [g], A. Mokhtarani [d], T. Montaruli [o,3], A. Morey [c], R. Morse [o], S. M. Movit [v], K. Münich [j], R. Nahnhauer [aa], J. W. Nam [k], P. Nießen [r], D. R. Nygren [d], H. Ögelman [o], Ph. Olbrechts [f], A. Olivas [i], S. Patton [d], C. Peña-Garay [s], C. Pérez de los Heros [x], D. Pieloth [aa], A. C. Pohl [x,4], R. Porrata [c], J. Pretz [i], P. B. Price [c], G. T. Przybylski [d], K. Rawlins [o], S. Razzaque [v], F. Refflinghaus [j], E. Resconi [aa], W. Rhode [j], M. Ribordy [q], S. Richter [o], A. Rizzo [f], S. Robbins [z], C. Rott [w], D. Rutledge [w], H.-G. Sander [p], S. Schlenstedt [aa], D. Schneider [o], D. Seckel [r], S. H. Seo [w], S. Seunarine [h], A. Silvestri [k], A. J. Smith [i], M. Solarz [c], C. Song [o], J. E. Sopher [d], G. M. Spiczak [t], C. Spiering [aa], M. Stamatikos [o], T. Stanev [r], P. Steffen [aa], D. Steele [o], T. Stezelberger [d], R. G. Stokstad [d], M. C. Stoufer [d], S. Stoyanov [r], K.-H. Sulanke [aa], G. W. Sullivan [i], T. J. Sumner [m], I. Taboada [c], O. Tarasova [aa], A. Tepe [z], L. Thollander [u], S. Tilav [r], P. A. Toale [w], D. Turčan [i], N. van Eijndhoven [y], J. Vandenbroucke [c], B. Voigt [aa], W. Wagner [j], C. Walck [u], H. Waldmann [aa], M. Walter [aa], Y.-R. Wang [o], C. Wendt [o], C. H. Wiebusch [z], G. Wikström [u], D. R. Williams [w], R. Wischnewski [aa], H. Wissing [aa], K. Woschnagg [c], X. W. Xu [o], G. Yodh [k], S. Yoshida [g], J. D. Zornoza [o] and P.L. Biermann [ab,ac]

[a] *CTSPS, Clark-Atlanta University, Atlanta, GA 30314, USA*

[b] *Dept. of Physics, Southern University, Baton Rouge, LA 70813, USA*

[c] *Dept. of Physics, University of California, Berkeley, CA 94720, USA*

[d] *Lawrence Berkeley National Laboratory, Berkeley, CA 94720, USA*

[e] *Université Libre de Bruxelles, Science Faculty CP230, B-1050 Brussels, Belgium*

[f] *Vrije Universiteit Brussel, Dienst ELEM, B-1050 Brussels, Belgium*

[g] *Dept. of Physics, Chiba University, Chiba 263-8522 Japan*

[h] *Dept. of Physics and Astronomy, University of Canterbury, Private Bag 4800, Christchurch, New Zealand*

[i] *Dept. of Physics, University of Maryland, College Park, MD 20742, USA*

[j] *Dept. of Physics, Universität Dortmund, D-44221 Dortmund, Germany*

[k] *Dept. of Physics and Astronomy, University of California, Irvine, CA 92697, USA*

[ℓ] *Dept. of Physics and Astronomy, University of Kansas, Lawrence, KS 66045, USA*

[m] *Blackett Laboratory, Imperial College, London SW7 2BW, UK*

[n] *Dept. of Astronomy, University of Wisconsin, Madison, WI 53706, USA*

[o] *Dept. of Physics, University of Wisconsin, Madison, WI 53706, USA*

[p] *Institute of Physics, University of Mainz, Staudinger Weg 7, D-55099 Mainz, Germany*

[q] *University of Mons-Hainaut, 7000 Mons, Belgium*

[r] *Bartol Research Institute, University of Delaware, Newark, DE 19716, USA*

[s] *Institute for Advanced Study, Princeton, NJ 08540, USA*

[t] *Dept. of Physics, University of Wisconsin, River Falls, WI 54022, USA*

[u] *Dept. of Physics, Stockholm University, SE-10691 Stockholm, Sweden*

[v] *Dept. of Astronomy and Astrophysics, Pennsylvania State University, University Park, PA 16802, USA*

[w] *Dept. of Physics, Pennsylvania State University, University Park, PA 16802, USA*

[x] *Division of High Energy Physics, Uppsala University, S-75121 Uppsala, Sweden*

[y] *Dept. of Physics and Astronomy, Utrecht University/SRON, NL-3584 CC Utrecht, The Netherlands*

[z] *Dept. of Physics, University of Wuppertal, D-42119 Wuppertal, Germany*

[aa] *DESY, D-15735, Zeuthen, Germany*

[ab] *Max Planck Institut für Radioastronomie, Auf dem Hügel 69, D-53121 Bonn, Germany*

[ac] *Department of Physics and Astronomy, University of Bonn, Germany*

Abstract

The sensitivity of a search for sources of TeV neutrinos can be improved by grouping potential sources together into generic classes in a procedure that is known as source stacking. In this paper, we define catalogs of Active Galactic Nuclei (AGN) and use them to perform a source stacking analysis. The grouping of AGN into classes is done in two steps: first, AGN classes are defined, then, sources to be stacked are selected assuming that a potential neutrino flux is linearly correlated with the photon luminosity in a certain energy band (radio, IR, optical, keV, GeV, TeV). Lacking any secure detailed knowledge on neutrino production in AGN, this correlation is motivated by hadronic AGN models, as briefly reviewed in this paper.

The source stacking search for neutrinos from generic AGN classes is illustrated using the data collected by the AMANDA-II high energy neutrino detector during the year 2000. No significant excess for any of the suggested groups was found.

Key words: Neutrinos, AGN, source stacking, point sources, AMANDA, IceCube
PACS: 95.55.Vj, 95.85.Ry, 98.54.-h, 98.70.Sa

1 Introduction

With AMANDA-II, different searches for high energy neutrino point sources have been performed [1,2,3], showing that neither the all sky search for hot spots in the neutrino sky nor the search at predefined and astrophysically motivated source positions has led to a discovery of a statistically significant neutrino signal. This however does not exclude the possibility that the signal of a superposition of generically equal sources, each contributing below the individual significance threshold, sums up to a significant signal for that specific source type. In case of no detection, the stacked signal may be used to obtain a limit on neutrino emission from that generic source type. Source stacking methods have been applied in gamma-ray astronomy, e.g., in searches for non-blazar AGN classes at GeV photon energies [4,5].

AGN belong to the most promising potential neutrino sources. Since the detailed mechanism of neutrino production in AGN is still unknown, in this paper a neutrino-production-model free attempt to classify the sources according to their geometrical properties and electromagnetic emission is introduced. Based on this classification, we develop an AGN stacking analysis to search for TeV neutrinos.

In Sec. 2, we describe in detail the adopted systematic classification of AGN based on an axisymmetric model [6]. Possible neutrino production scenarios in AGN are reviewed in Sec. 3. Pion production and subsequent decay results in correlated neutrino and photon production. Neutrino fluxes from these reactions are expected to be of the same order of magnitude as the gamma-ray fluxes. However, photons interact in the source environment possibly leading to a different photon spectrum than the neutrino spectrum. In Sec. 4, we define catalogs of AGN classes based on our classification, and select from them interesting neutrino candidate sources. Hence, we order sources according to their photon flux at different energies. In Sec. 5, a procedure is presented to

* Corresponding author. Contact: gross@physik.uni-dortmund.de
[1] Deceased
[2] affiliated with Institut für Physik, Humboldt Universität zu Berlin, D-12489 Berlin, Germany
[3] on leave of absence Università di Bari, Dipartimento di Fisica, I-70126, Bari, Italy
[4] affiliated with Dept. of Chemistry and Biomedical Sciences, Kalmar University, S-39182 Kalmar, Sweden

determine the optimum number of sources from each catalog to be included in the stacking analysis. This procedure is applied to determine source samples to be analyzed with the AMANDA neutrino telescope, located at the South Pole [7]. Thus selected sources in AMANDA's field of view are in the Northern sky. Assuming hypothetical distributions of the source strength as a function of the ordered source number we determine under which conditions a gain in sensitivity is obtained with the source stacking method with respect to other methods [1,8]. In Sec. 6, we illustrate our method by evaluating the signal from the resulting source samples using a data set collected by AMANDA in the year 2000 [1].

2 AGN classification

In this section we describe a possible classification of AGN useful to define catalogs of sources to be stacked. Historically, a large variety of AGN (like Seyfert galaxies, radio galaxies or quasars) have been named due to their appearance from Earth-based telescopes. The observational differences among the various AGN types can be partially explained with a geometrically axisymmetric model as the result of different inclination angles, defined as the angle between the line of sight and the AGN axis [6]. A pictorial scheme of an AGN showing the basic ingredients of the axisymmetric model is shown in Fig. 1. It consists of a rotating supermassive black hole, two jets with matter outflowing along the rotation axis and an accretion disk of matter perpendicular to the rotation axis. Aside from these geometrical differences, others will be outlined below.

We describe the AGN classification illustrated in Fig. 2 based on the morphology of the host galaxy, the luminosity and the inclination angle. AGN are generally divided into radio-loud and radio-weak sources as indicated in the first branching of the scheme. Radio-loud AGN (left branch of Fig. 2) can be classified according to radio jet lengths: compact objects, where the jets get stuck in dense matter [9], are discussed with more detail in Sec. 2.1 and AGN with fully evolved jets of a length of 100 kpc up to several Mpc in Sec. 2.2.

Typically, AGN spectra are composed of a thermal part, the so-called blue bump with the maximum at optical-UV frequencies, and a non-thermal part extending over up to 20 orders of magnitude in frequency. The blue bump is interpreted as thermal radiation of the warm inner accretion disk. The low energy component of the non-thermal spectrum in the radio to soft X-ray regime is assumed to be due to synchrotron radiation of electrons gyrating in a magnetic field. The origin of the high-energy component, if present, can be explained by hadronic or leptonic models (see Sec. 3). The non-thermal high energy photon emission is known to be highly variable on a wide range of time

scales, from less than one hour to months [10]. Within the thermal spectrum, some emission lines can be found.

Emission lines are classified as broad lines or as narrow lines. The axisymmetric model assumes that broad lines are due to fast moving dust clouds ($v \approx 1000$ km/s-5000 km/s) near the accretion disk. On the other hand, narrow lines originate in slowly moving dust clouds ($v \approx 500$ km/s) outside the torus. Depending on the angle of observation, the broad line emission from the clouds at the center may or may not be hidden by the torus. This model is confirmed by broad line observations in scattered light from some AGN, which show in direct light only narrow lines [11].

The radio emission of AGN is assumed to originate mostly in relativistic jets where it is caused by synchrotron radiation of electrons moving along the jet. AGN are called radio-loud if the ratio of the radio flux at 5 GHz to the optical flux is larger than 10 [6]. Radio-loud AGN are located in elliptical galaxies, while radio-weak AGN are located in spiral galaxies [12], and rarely in ellipticals.

Observations and jet models [13] show a flat radio spectrum for the flux density F ($F \propto \nu^{\alpha}, \alpha > -0.5$) [5] for the radio core, i.e. for the inner part of the jet. In contrast, radio lobes and hot spots located at the outer end of the jet typically show a steeper spectrum with spectral indices from -0.5 to -0.6 in hot spots and from -0.8 to -1.0 in lobes.

For the radio-weak AGN (right branch of Fig. 2), a luminosity dependent classification in optical wavelengths yields the division into quasars and Seyfert galaxies. The intrinsically stronger objects are the radio-weak quasars and the Radio Intermediate Quasars (RIQ) [14]. The radio-weak quasars are seen from moderate inclination angles ($20^{\circ} - 60^{\circ}$), the RIQ are interpreted as the same objects, but seen from smaller angles. The radio emission of RIQ is relativistically beamed, similarly to blazars (see Sec 2.2) [14]. The weaker objects are the Seyfert galaxies, classified as Seyfert I galaxies, if the core and the broad line region are visible, or Seyfert II galaxies, if the core is obscured by the torus [15]. Up to now, no Seyfert-like object with beamed emission has been observed.

[5] The spectral index α usually is determined between 2.7 GHz and 5 GHz.

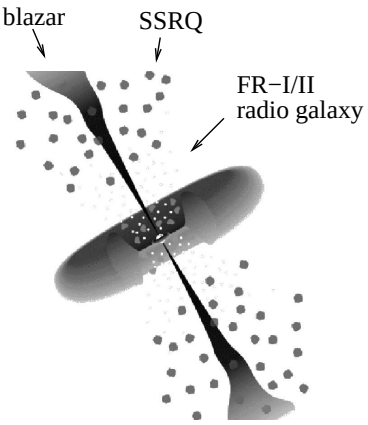

Fig. 1. Scheme of an AGN with a black hole in the center and an accretion disk perpendicular to the direction of two jets along its rotation axis. The different inclination angles of the line of sight with respect to the jet for blazars, steep spectrum radio quasars and radio galaxies are indicated by arrows. Image adapted from [6].

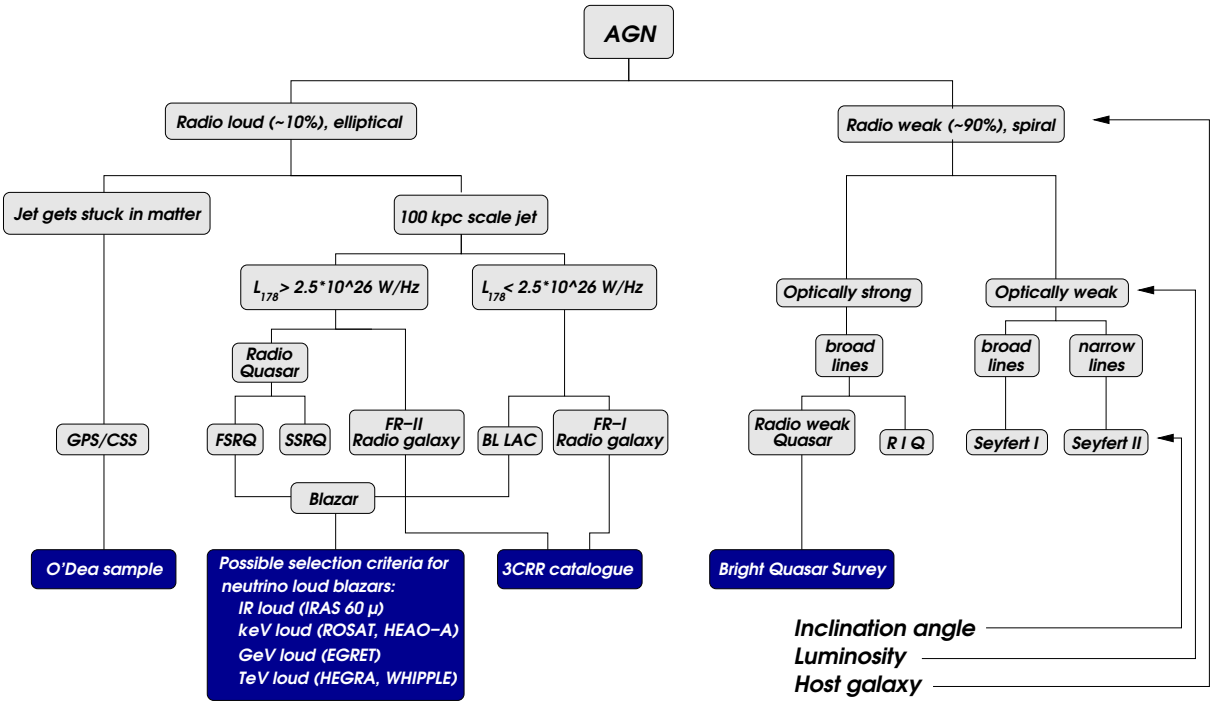

Fig. 2. AGN classification according to host galaxy, luminosity and inclination angle.

2.1 GPS and CSS

There is a substantial fraction of sources ($\approx 1/3$ when selecting the strongest sources at 5 GHz) which shows, for frequencies above a certain turnover value, a steep radio spectrum from the compact radio core. If the turnover is in the MHz range, the source is classified as *Compact Steep Spectrum* source (CSS), if it is in the GHz range, the source is a *GHz Peaked Source* (GPS). These

sources are significantly smaller than usual AGN: the GPS show linear sizes below 1 kpc, the CSS in the range of 1-15 kpc. GPS and CSS are not distinct source classes, since there is a continuous transition from the compact GPS to the slightly larger CSS. As pointed out in [9], the turnover frequency ν_m decreases with growing source size l as

$$\nu_m \propto l^{-0.65} \,. \tag{1}$$

The extremely high power of the GPS/CSS suggests a central engine similar to those of other AGN to provide sufficient energy.

The source compactness can be explained by the assumption that jets get stopped by interactions with dense matter. The most common interpretation of the turnover observed for this source class is the model of synchrotron self-absorption, although free-free absorption on thermal electrons is not excluded. The sharpness of the maxima found implies that the zone of the bulk radio emission is very small [16], presumably located at the outer end of the jet. GPS/CSS could be young states of radio-loud AGN evolving into larger radio sources. The population statistics of GPS/CSS and extended radio-loud AGN are in agreement with this picture, provided they stay in the compact state for a significant part of their lifetime.

For neutrino production, this class is of particular interest if proton acceleration takes place within the central part of the jet. As a matter of fact, the dense matter surrounding the source provides an ideal target for pion production. Since jets get stopped in the interaction zone, the predicted neutrino production is isotropic or only slightly beamed. Thus, the inclination angle is considered to have only small effects on the expected neutrino flux on Earth from this sources.

2.2 Radio-loud AGN with 100 kpc scale jets

Two different jet morphologies have been observed for radio-loud AGN with extended jets correlated with the radio luminosity at 178 MHz [17]. These AGN can be distinguished according to their luminosity: the critical value of the luminosity is $L_{178} = 2.5 \cdot 10^{26}$ W/Hz (see Fig. 2), corresponding to a bolometric luminosity of 10^{46} erg/s [18,19]. High luminosity AGN are characterized by powerful jets extending far outside the host galaxy. The increasing jet luminosity at the outer end produces extended radio lobes and the so-called hot spots. These objects appear as Flat Spectrum Radio Quasars (FSRQ), as Steep Spectrum Radio Quasars (SSRQ) or as FR-II radio galaxies [17]. Low luminosity AGN, divided in BL Lacs or as FR-I radio galaxies, have fainter jets. They show decreasing radio emission with growing distance from the

central black hole and have no hot spots.

This classification of radio-loud AGN assumes a typical value of the Lorentz factor $\gamma \approx 10$ for the bulk motion in the jet [6]. This value can also explain the apparent superluminal motion of radio knots in blazar jets [20].

Radio-loud AGN show different appearances for different inclination angles. This is due to the relativistic Doppler boost of the emission from the jet and the obscuration of the inner core by the torus. For large viewing angles to the jet axis (close to 90°), the torus obscures the inner part of the AGN. Hence, the broad line region and the thermal continuum radiation of the accretion disk cannot be seen. In this case, the AGN is called a *radio galaxy*.

If the opening angle of the torus is large enough, there is a range for the inclination angle, where the inner core is visible and the relativistic Doppler factor is smaller than 1. In this case the core is seen with its blue bump from the inner accretion disk and broad emission lines are present in the spectrum. The radio spectrum of these objects is still steep and lobe-dominated. Only high luminosity objects show this morphology, then appearing as SSRQ with a bright optical core and strong broad emission lines. The lack of similar low luminosity objects is still a matter of debate. Possibly, the inner core is obscured by the torus until the inclination angle is so small that the emission becomes Doppler boosted [19].

For very small inclination angles ($\lesssim 12°$), the jet radiation is Doppler boosted due to the relativistic motion of the bulk outflow towards the observer. These objects are characterized by a flat radio spectrum, strong variability and polarization. FSRQ and BL Lac objects can be combined into the blazar class since both are characterized by strong beaming effects. The flat radio spectra of blazars can be explained by the dominance of the boosted flat-spectrum core over the non-boosted steep-spectrum radio lobes and will be used as selection criterion for blazars. A flat spectral index in radio is an indication of optical thickness [13].

BL Lac objects are low-luminosity objects with a FR-I type jet, while FSRQ are considered as the high luminosity objects (FR-II jet). The BL Lac objects are commonly divided into high-energy cutoff BL Lac (HBL) and low-energy cutoff BL Lac (LBL), referring to the maximum energy of the electron synchrotron spectrum. HBL are relatively weak in radio flux, strong in X-ray flux and bolometrically less luminous than LBL. A distinction between these classes is usually made by taking into account whether the radio-to-X-ray spectral index α_{rx} (with $F(\nu) \propto \nu^{\alpha_{rx}}$) is bigger (LBL) or smaller (HBL) than -0.75 [6]. The high energy γ emission of HBL and LBL differs: all confirmed AGN TeV sources are HBL[6] [21]. In contrast, the stronger AGN GeV (EGRET)

[6] However, there are indications of TeV radiation from BL Lacertae (LBL) and

sources consist of LBL and FSRQ, and only 2 of the 6 confirmed TeV γ AGN have been detected by EGRET, with only moderate fluxes [22].

3 Selection of neutrino source candidates

Accelerated proton interactions with ambient photons or matter lead to neutrino production through the reactions:

$$
\begin{aligned}
& p\gamma \to \Delta^+ \to n\pi^+ \\
& pp \to \pi^\pm + N \\
& \qquad \pi^\pm \to \mu^\pm \nu_\mu \to e^\pm \nu_e \nu_\mu \nu_\mu \,,
\end{aligned}
$$

and similar reactions for neutrons. These processes are always accompanied by neutral pion production. Neutrino and gamma ray fluxes are expected to be of the same order of magnitude. Since in most scenarios, proton and target photon spectra fall steeply with energy, higher resonances and multi-pion production represent a small correction to pion production. The acceleration of the protons is assumed to be due to shock acceleration which may take place in the relativistic jet [20,23] or in the accretion disk [24,25]. Due to low plasma density in AGN jets, the $p\gamma$ interactions are likely to be dominant over pp [20]. This is also indicated by the lack of absorption lines in AGN X-ray spectra [26]. An exception from this consideration is given, if pp interactions take place at the inner edge of the accretion disk [25].

If acceleration takes place in the disk, electromagnetic cascades initiated by photons from neutral pion decay would lead to a non-thermal X-ray spectrum. However, measured AGN X-ray spectra and the diffuse X-ray flux show the dominance of a thermal flux peaked around 100 keV [27]. This discrepancy might be solved by assuming that the non-thermal X-ray spectrum contributes only 30% to the measured X-ray flux [26]. That implies that hadronic interactions are not dominant. Hence, the resulting neutrino spectrum would be reduced by the same factor. Due to this discrepancy, the disk model is disfavored as a dominant process for neutrino production.

For the jet as well as for the disk, the theory of diffusive shock acceleration suggests a power law spectrum with a differential spectral index $\alpha \approx 2$ for protons [28,29,30]. Neutrinos and photons are produced with the same index if multi-pion production is not dominant. However, the energy of photons produced by neutral pion decay may be redistributed to photons of lower energy by synchrotron pair cascades. The photon escape energy depends on

M87 (misaligned BL Lac or FR-I) weakening the association.

the optical depth. Hence, the spectra of neutrinos and photons can differ considerably, while the bolometric luminosity remains correlated [31].

Hadronic jet models have been proposed to explain the high energy γ emission from the jet. A comparison to purely leptonic models can be found in [20]. Purely leptonic models usually explain the high energetic (TeV) radiation by inverse Compton scattering of photons. Models in which the photons originate as synchrotron radiation are classified as Synchrotron Self Compton (SSC); those in which the photons are ambient are classified as External Compton (EC). The EC model requires high densities of external photons to be Compton up-scattered to higher energies. These photon densities then constrain the escape energy of photons to values below 300 GeV. Thus, the leptonic EC model cannot explain the observed TeV sources [20]. In the SSC models, the ratio between GeV and radio luminosity is constrained, predicting a larger number of GeV blazars than observed by EGRET. Additionally, keV and TeV fluxes are correlated. Many observations confirm these correlations and apparently favor the SSC model. However, recent observations indicate the existence of orphan flares for 1ES 1950+650 [32] and for Mrk 421 [10,33], where the TeV flux flares but the X-ray flux does not.

In hadronic models, the emission of high energetic photons in the jet is not assumed to be directly from photohadronic processes. A non-negligible optical depth makes TeV photons cascade to lower energies. Thus, an additional mechanism for high energy gamma production is necessary. In proton initiated cascade models (PIC), it is assumed that electrons scatter on some target photons acquiring higher energies. In the SS-PIC (self synchrotron PIC) model, the target photons are those emitted in the cascades. The EC-PIC (external Compton PIC) assumes external photons to be scattered up to higher energies by the inverse-Compton process [20].

Another possibility to explain observed high energy γ emissions is given by the Synchrotron-Proton Blazar model proposed by Mücke and Protheroe [34]. It assumes relativistic protons to emit synchrotron radiation at higher energies than the one from gyrating electrons. This model explains the observed double hump energy spectrum and predicts neutrino emission spectra for HBL and LBL [35]. The emission of TeV γ-rays via synchrotron radiation requires protons to reach extremely high energies, which is possible only if the interaction rate is sufficiently low. Hence, in TeV emitters $p\gamma$ and pp interactions must be less frequent than in blazars without intense TeV photon emission. This results in predictions of neutrino fluxes for HBL being 6 orders of magnitude less than for LBL.

In summary, to select source candidates, we assumed the common origin of neutrinos and photons from pion decay and the classification described before. Since the optical depths of AGN are unknown, escaping photons can be of

significantly lower energy. This is taken into account by the selection of source candidates at various energies where data are available (radio, IR, optical, keV, GeV, TeV). Moreover, we assume that the observed photon flux is proportional to the TeV neutrino signal. While this selection does not depend on detailed AGN models, other explicitely model dependent selections are possible, e.g. based on the concept of the jet-disk symbiosis [13,18] used in [36].

4 Selection of neutrino candidate sources from catalogs of AGN classes

We consider catalogs of AGN classes and apply some selection rules, described in Tab. 1, in order to obtain 'statistically complete catalogs' of sources in a well-defined part of the sky above a flux threshold. In this selection we did not consider the variability in time of emissions from AGN. As a matter of fact, most of the available photon data were not collected at the same time as the considered AMANDA data set. Future multi-wavelength campaigns and simultaneous collection of photon and neutrino data will allow approaches that also account for time dependencies.

To all the considered catalogs we applied the requirement that the galactic latitude b is larger than 10° (except for radio-weak quasars, where the catalog itself requires $|b| > 30^\circ$). This cut excludes the galactic plane in order to avoid biasing AGN samples with galactic sources. Moreover, a minimum declination of 10° is required since we look for neutrino induced upgoing muons. We also consider a threshold on the distance corrected flux, to exclude intrinsically weak nearby sources which might otherwise migrate into the catalog due to their distance. The formula used for the correction is given in appendix A. We stress that some blazar sources have been removed from our catalogs by a cut on the distance corrected flux. The sources that were removed only due this cut are listed in Table B.11. Among these there are some well-known nearby AGN, e.g. NGC 1275 would be in the IR-blazar and in both keV-blazar samples and Mrk 501 would be in both keV samples. The occurrence of these sources in various samples confirms our assumption that these sources migrate into the samples due to their proximity and should not be considered as generic sources. These nearby sources with such high fluxes would bias a stacking analysis, hence they should be analyzed as individual sources [1].

In the following sections we describe with more details the catalogs for the considered classes of sources in Tab.1 to which we apply selection rules. Then we consider for which of these selected sources there exist measurements of the photon flux that we assume to be correlated to neutrino fluxes and give our lists of candidate neutrino sources for the various classes.

Sample	Flux /luminosity cuts	Coordinate cuts	Further cuts
Blazars	$F_{5GHz} > 0.8$Jy, $F_{5GHz}^{z=0.1} > 1.5$ Jy	$\delta > 10°, \|b\| > 10°$	$\alpha > -0.5$ with $F_\nu \propto \nu^\alpha$
CSS	$F_{178MHz} > 10$Jy, $\log P_{178MHz} > 26.5$	$\delta > 10°, \|b\| > 10°$	Lin. size$<$ 20kpc
GPS	$F_{5GHz} > 1$Jy, $\log P_{5GHz} > 26.5$	$\delta > 10°, \|b\| > 10°$	0.4GHz$< F_{max} <$ 6GHz
FR-I	$F_{178Mhz} > 10$Jy, $L_{178MHz} < 2.5 \cdot 10^{25}$ W/Hz	$\delta > 10°, \|b\| > 10°$	
FR-II	$F_{178Mhz} > 10$Jy, $L_{178MHz} > 2.5 \cdot 10^{25}$ W/Hz	$\delta > 10°, \|b\| > 10°$	
QSO	$B < 16.16$, $U - B < -0.44$	$\delta > 10°, \|b\| > 30°$	

Table 1
The selection criteria defining catalogs of the different source classes. F_ν stands for the photon flux at a certain frequency ν in Jy, $F_\nu^{z=0.1}$ is the distance corrected flux to a redshift of $z = 0.1$, $\log P$ is the logarithmic power in W/Hz and L is the luminosity. The declination is labeled as δ while b stands for the galactic latitude. For the blazars, the spectral index α is determined between 2.7 GHz and 5 GHz. For CSS selected at 2.7 GHz, a back-extrapolation of a steep spectrum component to 178 MHz was used instead of the measured 178 MHz flux. U is the magnitude of the UV flux (λ = 300 nm−400 nm), B the magnitude of the flux at λ = 400 nm−550 nm (blue).

4.1 Blazars

As explained in Section 3, blazars are characterized by a flat radio spectrum, which we use as the selection criterion here to create a 'blazar list'. For radio sources with high fluxes at 5 GHz (λ = 6 cm), Kühr et al. [37] worked out a complete catalog of radio sources with flux larger than about 1 Jy [7]. A second version also covers sources below this threshold, using data available up to 1981 [38]. In the Northern sky, this catalog contains the "strong surveys" S1-S5 with a threshold of 0.8 Jy and below. The selection rules select from the blazar catalog about 150 sources.

Since blazar jets are in the direction of the observer, blazars are interesting candidate sources of neutrinos that could be produced in the jet. Corresponding to different assumptions on the optical depth of blazar jets, the neutrino flux is assumed to be proportional to the photon flux that are measured by various experiments in different energy ranges: HEGRA and Whipple in the

[7] 1Jy = 10^{-26}Ws^{-1}m^{-2}, in older papers also called f.u. for flux unit.

TeV one, EGRET in GeV, HEAO-A and ROSAT in keV or IRAS in infrared. The ordering of the sources is done according to the flux value in the relevant energy range. For the resulting samples, the relative source strengths at the selection energies are displayed in Fig. 3(a). The flux of the strongest source is normalized to 1.

For the sources in our list we look for catalogs of the measured photon flux in various bands to order them according to their photon emissions.

IR-loud blazars: the Infrared Astronomical Satellite (IRAS) provides a survey at wavelengths 12μm, 25μm, 60μm and 100μm. The Faint Source catalog IRAS F, covering most parts of the sky outside the galactic plane, includes 173,044 sources [39]. We find in total 12 sources in the IRAS F catalog that satisfy our selection criteria and match sources in our original 'blazar list'. The IR selected sample is given in Table B.1.

X-ray blazars: in the X-ray regime, there are only a few all-sky surveys. We make the hypothesis that soft and hard X-ray emissions are positively correlated with TeV neutrino production. For hard X-rays (0.25-25 keV) there exist only the HEAO-A measurements performed in the 1970s with low sensitivity and relatively poor angular resolution. This resulted in the 1H catalog [40] containing 842 sources. The X-ray satellite ROSAT performed an all-sky survey in the 0.2-2 keV band, with high sensitivity and good angular resolution in the range of a few tens of arc-seconds. The strongest sources found in the all-sky survey are listed in the 1RXS catalog [41], which contains in total 18,811 sources. For these antipodal satellites, two separate candidate lists are constructed from 1RXS and 1H sources that match our 'blazar list'. This resulting selections are listed in Table B.3 for HEAO-A and in Table B.2 for ROSAT.

GeV blazars: in the GeV range, the most sensitive data are those collected by the EGRET experiment on board the CGRO satellite [42]. The third EGRET catalog (3EG) [22] contains in total 271 sources of which 66 have been identified as blazars and additional 27 sources with lower confidence. We select EGRET sources that are reliably identified with a blazar in our list (class 'A' in the 3EG catalog), while weakly identified sources (class 'a' in the 3EG catalog) are accepted if an independent analysis confirms this identification [43]. The sources are sorted according to the maximum flux detected by EGRET. This yields the source subsample observable by AMANDA presented in Table B.4.

We include a further sample (see in Table B.5) selected among the unidentified EGRET sources (these have not yet been identified with sources detected at other wavelengths). Although a large fraction of these sources is likely to be galactic, some may be extragalactic. To select presumably extragalactic sources, aside from the usual galactic plane exclusion, we check that sources do not show features typical for galactic [8] sources. Selected sources are listed in Table B.5. These sources show a high variability, even higher than that of the identified AGN, and a large energy output that can be explained, even if they are also AGN.

TeV blazars: up to now, only 6 blazars have been firmly detected emitting TeV photons, of which 5 are in the field of view of AMANDA [21]. All TeV blazars show extreme variability in flux, such that a flux ranking becomes impossible. The sources all have a quite weak radio flux and do not fulfill our radio selection criteria for blazars. Furthermore, due to absorption by the IR background, only nearby sources can contribute to the TeV photon flux. These conditions prevent the use of our selection scheme for TeV blazars. But since in optically thin sources, TeV photons are strictly correlated to TeV neutrinos, we consider all observable TeV blazars, listed in Table B.6, for the source stacking analysis.

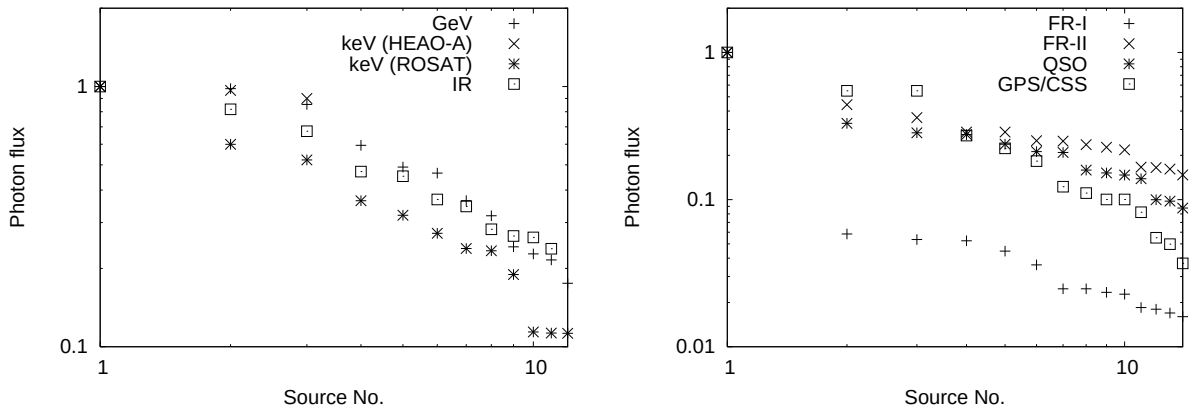

(a) (b)

Fig. 3. Relative strength at the selection energy of strongest sources in blazar samples (a) and in non-blazar samples (b).

[8] Three different types of presumably galactic sources have been considered: two are concentrated on the galactic plane with $|b| < 5^\circ$, while the third is associated with the Gould belt [44]. The latter form the so-called Local Gamma-Ray Population characterized by constant fluxes below $2.4 \cdot 10^{-7} \mathrm{s}^{-1}\mathrm{cm}^{-2}$ and a soft spectrum (photon spectral index $\gamma \approx 2.45$); they reach galactic latitudes up to 30°.

4.2 GPS and CSS

For defining a catalog of compact sources, we follow the selection of O'Dea [9]. The catalog contains former selections of CSS by Fanti et al. [45] and of GPS by Stanghellini et al. [46]. Since CSS and GPS are characterized by a maximum in the radio flux at a size-dependent frequency, the selection of these sources is done at several frequencies: 178 MHz, 2.7 GHz and 5 GHz depending on the peak location.

From the original CSS samples, all sources have been removed which do not fulfill all the selection criteria in the original paper [45]. The same has been done for CSS and GPS sources when the requirements of the more recent analysis [9] are not fulfilled. Additionally, we put a cut on the absolute power at 5 GHz, similar to the cut on the power at 178 MHz for the CSS sources indicated in Tab. 1. The typical spectra of sources are plotted in Fig. 4. In total 40 sources are selected of which 9 are GPS, 23 are CSS and 8 sources fulfill selection rules for both classes.

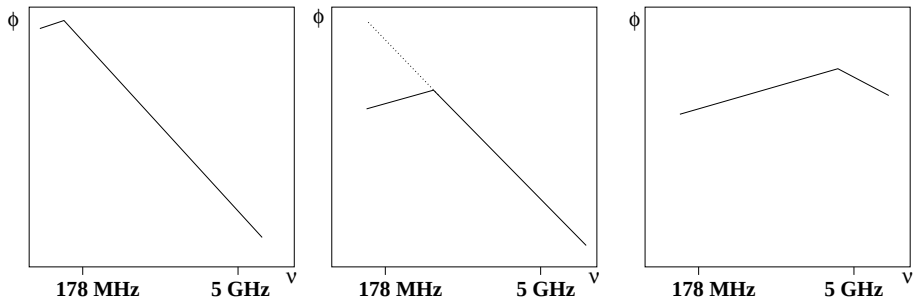

Fig. 4. Schematic plot of radio spectra of sources fulfilling the CSS and GPS selection rules. On the left: a typical spectrum of a CSS selected at 178 MHz. In the middle: a CSS spectrum with the maximum near 2.7 GHz. On the right: a GPS spectrum selected at 5 GHz. For the sources selected at 2.7 GHz, the back-extrapolation of the steep spectrum component to 178 MHz is relevant for the selection.

Since CSS and GPS were selected at three different radio frequencies, we cannot use the intensity in the radio. Since there are only few X-ray or IR data for these sources, the only possibility to get a suitable source ranking is to use data in the optical band taken from [9]. The underlying hypothesis we make is that the TeV neutrino flux is proportional to the optical flux. Our resulting neutrino source catalog is displayed in Table B.7.

4.3 FR-I and FR-II-radio galaxies

As the distinction between FR type I and type II radio galaxies is made at 178 MHz, it is adequate to select radio galaxies from observations at this

frequency. Data at this frequency can be found in the 3C catalog in its revised version (3CRR) [47]. The classification into FR-I and FR-II galaxies depends on the availability of the redshift for the source and is taken from [48]. The selection results in a catalog of 24 FR-I and 122 FR-II galaxies. Additionally, 16 compact sources fulfill the selection. They belong to the CSS source class as discussed in 4.2 above and are removed from the FR-I and FR-II samples.

For the selection of the neutrino candidate list, the radio flux at 178 MHz is assumed to be proportional to the TeV neutrino flux. Hence, we use these fluxes to sort the samples of radio galaxies. The results are listed in Table B.8 for FR-I and in Table B.9 for FR-II galaxies. Since FR-I/II radio galaxy jets do not point towards us, the observable neutrino flux produced in the jets is expected to be weaker for these sources than for blazars. Nonetheless, neutrino production in the disk is expected to be isotropic compared to the case of jet emission. This enhances the observation probability since it is not required that the observer is in the direction of the jet.

4.4 Radio-weak Quasars

A complete catalog of quasars selected at optical to UV wavelengths is given by the *Bright Quasar Survey* (BQS) [49]. A quasar is identified by an excess of UV flux. The catalogs presented by Sanders et al. [50] contain in total 109 sources, of which 59 sources are radio-weak quasars in the sky viewable by AMANDA.

Multi-wavelength investigations of the BQS sample show a second maximum in the photon spectrum at IR wavelengths for some of the quasars [50]. Hence, in the usual assumption that photon flux features are correlated to neutrino production at the source, we include in our list the radio-weak quasars selected according to their photon flux at 60 μm. The full quasar catalog selected from the BQS according to the IR flux is given in Table B.10.

For the resulting samples of CSS/GPS, FR-I/-II radio galaxies and radio-weak quasars, the relative source strengths at the selection energies are displayed in Fig. 3(b). The flux of the strongest source is normalized to 1.

5 Optimization of the number of sources and the bin size

5.1 The statistical optimization procedure

The different hypotheses on the neutrino flux from the sources in our catalogs determine the relative source strength within each class but leave the normalization free. We have normalized the signal by relating the sensitivity of the point source analysis to the signal of the strongest source in each sample. We consider here data taken by AMANDA during the year 2000 [1].

In the point source analysis, a search was performed for a statistically significant excess from any direction. For this purpose, any position on a grid of rectangular search bins is evaluated by considering the background expectation calculated from the average number of events in the corresponding zenith range. No point sources were detected; the observed excesses were equivalent to those in a randomized distribution. In the considered data set, we find by multiplication of the sensitivity[9] with the effective area, the lifetime of the analysis [1] and the bin efficiency for a circular search bin of 3.5° radius that the sensitivity (90% C.L.) corresponds roughly to three neutrinos in a 3.5° bin. This motivates the choice of the normalization of the neutrino flux for the most intense source that would produce a neutrino signal $S_1 \leq 3$ events in the considered AMANDA data set. Hence, for this source stacking analysis, we optimized the number of sources using $S_1 = 1, 2, 3$ events (also using the bin efficiency for 3.5°). Significantly higher signal normalizations would imply that the most intense source must be correlated with the position of a few spots, where an excess has been observed. These excesses are most probably due to statistic fluctuations. Since we do our selection independent of the results from that data set, such a coincidence is not assumed. On the other hand, for $S_1 < 1$, the expected signal is too faint to result in a notable contribution in the source stacking analysis. For the small numbers considered, Poisson statistics has to be applied. With our normalizations, the assumed neutrino fluxes for the sources in our catalogs agree with the limits of the current diffuse analyses [51,52].

Since the sensitivity of the AMANDA-II detector is almost independent of the declination, in the optimization procedure we approximate the background to be constant in the considered declination range. A total amount of 699 events in the year 2000 neutrino sample results in a background of 111.25/sr for that year.

A given number of sources N_{src} corresponds to a mean number of expected signal events, S, and a mean number of expected background events, BG.

[9] We define the sensitivity as the average upper limit in case of no signal.

Using Poisson statistics, we optimize for the median significance which will be reached in 50% of the experiments being performed under these assumptions. First, we calculate the median number of events n under signal hypothesis as a function of the number of sources to be included. Then we calculate the Poisson probability to observe at least n events with the assumption of pure background. Rescaled to the corresponding number of standard deviations of a Gaussian, δ, we get the median significance as a function of the number of sources to be included. The optimum number of sources, as determined by this median significance procedure, corresponds to the highest value of δ.

The same procedure is applied to the size of circular search bins, varying the signal according to the point spread function (PSF) and the background according to the area covered by the search bins. The PSF is evaluated for the most likely case of an E^{-2} spectrum. Since the PSF is not completely independent of the declination, we use the PSF averaged over all declinations. In Fig. 5 the average PSF obtained by considering an isotropic source distribution over the sky with $\delta > 10^{\circ}$ is plotted for various spectral indices. The declination dependence of the median of the PSF is shown in Fig. 6 for an E^{-2} spectrum. The resolution slightly improved for larger values of the declination.

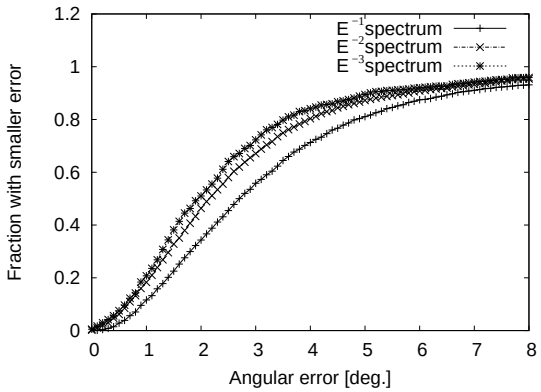

Fig. 5. Cumulative Point Spread Function after quality cuts for various spectral indices in year 2000 sample.

The optimum number of sources and the optimum bin size are not independent of each other. Thus, we follow an iterative procedure. First we evaluate the number of sources with rough estimates for signal and background. Then we optimize the bin size for the given number of sources, and finally, we check the number of sources again.

The results for the optimum values have been checked by a second procedure which will be called maximum observation probability procedure. A minimum significance δ was predefined and the probability to observe at least this significance is optimized. As the expected signal is rather small, a value of 3σ was chosen for δ.

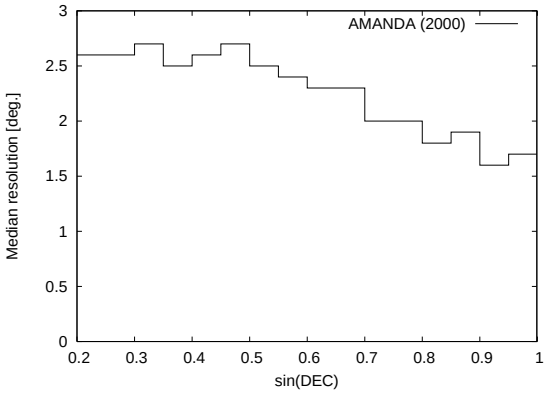

Fig. 6. Median PSF of AMANDA for data collected in 2000 as a function of $\sin(DEC)$.

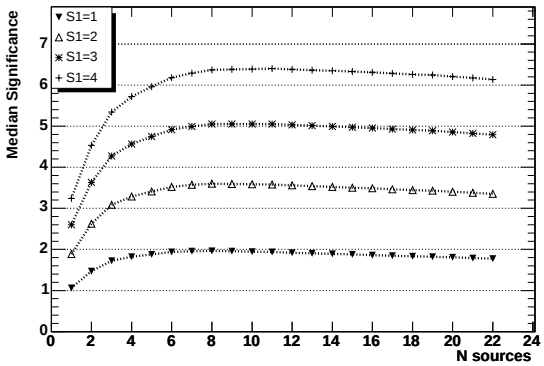

Fig. 7. Median significance as expected under the considered hypothesis as a function of the number of GeV blazars to be stacked. The highest value of the median significance corresponds to the optimum number of sources.

5.2 The resulting samples

We use the total number of events and the PSF from the year 2000 point source sample [1] for the optimization to determine samples from our catalogs to be analyzed for a cumulative neutrino flux. Our procedures may be applied to other data sets easily. The resulting parameters for year 2000 data are listed in Table 2.

In Fig. 7, we plot the median significance as a function of the number of EGRET blazars to be included for signal normalizations S_1 ranging from 1 to 4. The highest normalization of $S_1 = 4$ signal events from the strongest source is unlikely, as it implies a median significance above 3σ for the single source search. Hence, $S_1 = 4$ has not been taken into account when evaluating the optimum.

For most source classes, we find an optimum of about 10 sources. With one

exception, the source stacking analysis is more sensitive in testing the corresponding hypotheses than the point source analysis of single sources. Usually, the observed peaks are asymmetric: if more sources than the optimum number are included, the expected significance falls only slowly. On contrast the significance falls quite steeply if fewer sources are included.

The exceptions are found for FR-I and for FR-II radio galaxies, where the results are completely different. As there is a luminous FR-I galaxy in our neighborhood, M87, the whole FR-I flux would be strongly dominated by M87. The detection of TeV photons from this non-blazar AGN by HEGRA [53] and H.E.S.S. [54], theoretically predicted in [55], also supports the uniqueness of this source. Thus, the optimization suggests just to analyze the neutrino flux from that source only. In other words, the analysis of the strongest source only is more sensitive to our hypothesis than source stacking for the corresponding catalog. However, for two reasons we decided to analyze additionally a FR-I sample without M87. First, there is always the possibility that a single source does not contribute to the neutrino flux due to a reason not considered at selection. Second, in the opposite case, if M87 would be identified as a neutrino point source, the cumulative signal of the other sources contains information whether the M87 neutrino flux would be a specific feature of that source or a general characteristic of FR-I galaxies. Thus, we analyze a FR-I sample without M87 additionally. Then we find an optimum value of 20 sources to be included.

The situation of FR-II galaxies is opposite to that of FR-I galaxies. There are a lot of sources at higher redshifts with similar luminosities. This results in an monotonically increasing sensitivity while including more sources. Eventually, the coverage of the sky by search bins reaches a significant fraction of the sky and the techniques of point source analysis become less suitable to analyze the signal. If the energy spectrum of the signal differs from the atmospheric background, diffuse techniques searching for global excess of high energy neutrinos should be more sensitive to FR-II galaxies. However, since point source analysis and diffuse analyses are using complementary techniques and a point source analysis can give more information about the origin of the excess, a source stacking analysis of FR-II galaxies may also be useful. Since our optimization fails, we have to define the most suitable value for the number of FR-II sources to analyze. For that, we use a local saddle point at 17 sources for the cutoff where the sensitivity grows only marginally if further sources are included.

The unidentified EGRET blazars show nearly constant values for observation probability and median significance between 15 and 35 sources.

The hard X-ray sources are restricted to three sources due to the poor sensitivity of HEAO-A, an experiment of the 1970s.

We cross-checked the procedure based on the mean significance to that based on the maximum observation probability. The deviations between the results from the two procedures are within the corresponding uncertainties of the determination of the optimum.

For the optimum bin size, we find results between 2.6° for the unidentified GeV sources and 3.0° for the single source M87. As expected [56], the bin size decreases with the size of the sample.

source class	N_{src}^{MS}	N_{src}^{DP}	**listed in**	**Bin size [deg.]**
IR blazars (IRAS)	11^{+0}_{-1}	11^{+0}_{-1}	table B.1	2.8 ± 0.2
keV blazars (ROSAT)	8 ± 1	9 ± 1	table B.2	2.8 ± 0.2
keV blazars (HEAO-A)	3 ± 0	3 ± 0	table B.3	2.9 ± 0.2
GeV blazars	8 ± 1	9 ± 1	table B.4	2.8 ± 0.2
unidentified GeV sources	22 ± 5	20 ± 5	table B.5	2.6 ± 0.2
TeV blazars	5^*	5^*	table B.6	2.8 ± 0.2
GPS and CSS	8 ± 1	8 ± 2	table B.7	2.8 ± 0.2
FR-I radio galaxies	1 ± 0	1 ± 0	table B.8	3.0 ± 0.2
FR-I without M87	20^{+3}_{-5}	19 ± 4	table B.8	2.6 ± 0.2
FR-II radio galaxies	122	$17^{+105}_{-5}{}^{**}$	table B.9	$2.6 \pm 0.2^{***}$
Radio-weak quasars	11^{+1}_{-3}	11^{+1}_{-3}	table B.10	2.8 ± 0.2

Table 2
Resulting parameters for the source stacking analysis.
N_{src}^{MS} and N_{src}^{DP} stand for the optimum number of sources determined with the median significance procedure and, respectively, the maximum observation probability procedure.
* All sources included without optimization, see above .
** This value was taken for the analysis. Only a saddle point. The observation probability increases again, when including all sources (→ diffuse analysis). See Sec. 5.2.
*** Bin size evaluated for 17 sources.

5.3 The relation between flux distribution and the optimum number of sources

As described above, the optimization of the number of sources can lead to two special cases, where either the source stacking analysis degenerates to a point source analysis of a single candidate source, or to a diffuse analysis where the arrival direction of the neutrino becomes irrelevant. If the flux falls only slowly from the strongest source to the weakest, as is the case for FR-II

radio galaxies, then we cannot find an optimum number of sources. So the probability to observe a signal always increases when more sources are added. In the other extreme, as was found for FR-I radio galaxies, if the strongest source is expected to contribute most of the flux and the other sources are substantially weaker, then the sample of sources to be stacked degenerates to a single source. Here we investigate the conditions on the flux distribution for these degeneracies to occur. We consider the flux F of the N^{th} source, $F(N)$. Motivated by the nearly linear decrease of $F(N)$ in the double logarithmic plots in Fig. 3, we assume a power law,

$$F(N) \propto N^{\alpha} \,. \tag{2}$$

For $\alpha \geq -1$, the finiteness of the total flux requires a cut-off or a steepening.

For different values of α, we evaluate the optimum number of sources and determine the range of values for α, where the two degeneracies occur. The maximum number of considered sources is set to 100. This corresponds to a coverage of about 10% of the sky viewable by AMANDA, assuming a bin size of 2.6° . For significantly more sources, the sky get densely covered by candidate sources and the directional information cannot be used and diffuse methods are more useful.

For a slowly falling flux distribution with $\alpha > -0.65$, we cannot find an optimum number and all sources have to be included. In the range $-0.65 > \alpha > -2$, a non-degenerate optimum number of sources is found and for $\alpha < -2$, only the strongest source has to be selected. The thresholds depend on the detector parameters, although for $\alpha > -0.5$, $S/\sqrt{BG}$ diverges, i.e. the degeneracy occurs generally for these values. An improved angular resolution can explore the range $-0.65 < \alpha < -0.5$ for a source stacking analysis.

A fit of α on the flux distributions of our samples results in $\alpha = -0.6$ for FR-II radio galaxies and for IRAS blazars, a 2-point index $\alpha = -4.1$ for the two strongest FR-I radio galaxies and $-0.7 \geq \alpha \geq -1.1$ for the other samples. For all samples, the results of the optimization are in agreement with our classification according to α.

6 The results for the year 2000

The sources we selected are listed in Table B.4-B.10 in the appendix. We apply the source stacking method to the data collected by AMANDA in the year 2000 using the event sample from the previous point source analysis [1] corresponding to a detector lifetime of 197 days. The selection of well reconstructed events was optimized for high sensitivity to point sources. In Fig. 8,

the reconstructed arrival directions of the individual events of this data set are shown in a sky map. The zenith distribution of these events is displayed in Fig. 9 in comparison with the simulated angular distribution of atmospheric neutrinos. Since the event selection was not optimized for purity, the excess of measured events close to the horizon is expected as the contribution of poorly reconstructed atmospheric muons. The detector response with this event selection was simulated for various spectral indices. The energy spectrum folded with the Earth absorption factor and with the detector response is shown in Fig. 10. A uniform source density on the Northern Sky was used in the simulation, corresponding to a mean zenith angle of 33.4°. For an E^{-2} power law spectrum, as expected from Fermi acceleration, that means 90% of the signal events are between the AMANDA energy threshold at 50 GeV and 350 TeV.

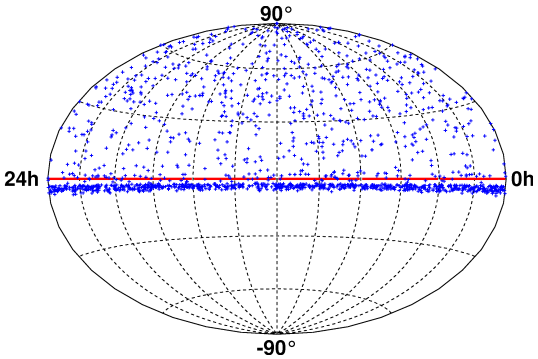

Fig. 8. Reconstructed arrival direction of 1557 selected events in the year 2000 sample [1]. The events below $\delta = 0°$ are dominated by atmospheric muons.

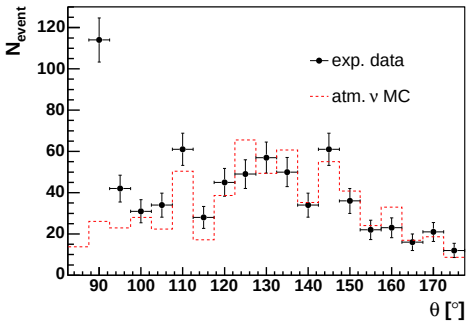

Fig. 9. Distribution of the zenith angle in the considered data set in comparison with the expectation of atmospheric neutrinos from simulations.

Results obtained on a more complete set of data collected in the years 2000-2003 will be reported in [3]. Moreover, this method and the list of sources we derived will serve as the starting point for stacking analyses performed with the IceCube neutrino telescope [57] which is currently under construction. AMANDA will be integrated into IceCube. The source stacking method will be adapted to the better performance of the larger detector in terms of effective area and angular resolution. Application of this method for other neutrino telescopes [58,59,60,61,62] is conceivable.

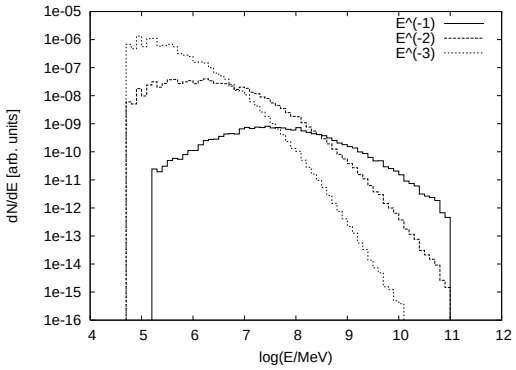

Fig. 10. Energy spectra folded with the response of the AMANDA detector for hypothetical source spectra with the spectral indices -1, -2 and -3.

In this analysis, only the cumulative result for a class of sources is evaluated, not the signal for individual sources. The AMANDA collaboration follows a strict blindness policy, i.e. an analysis has to be developed blindly with respect to the data. This prevents statistical fluctuations to affect the final steps of the analysis. In the context of the source stacking analysis, the selection of sources was done independently of the AMANDA data itself. No signal was evaluated until the source samples and all analysis parameters were fixed.

The number of observed events in our search bins has to be compared with the background, mainly atmospheric neutrinos. Since the background is independent of the right ascension, for each position in the sky it can be evaluated from the events in the same declination band. If two sources of the same sample are very close to each other, their search bins may overlap. Then, the background expectation is corrected for the overlap and events in the overlapping area contribute only once to the cumulative signal.

The probability to observe the measured number of events under the hypothesis of pure background is evaluated by Poisson statistics. The correctness of the analysis was tested with two procedures. First, to test the correct evaluation of the significance, a collection of data sets with randomized right ascension was created and the significance of the signal from the stacked sources in these randomized data sets was determined. As expected for randomized data sets, the significance follows a Gaussian with a width of one centered at zero. Additionally, hypothetical source lists with random source positions were evaluated using the original data set. The results of the point source analysis of the considered data set [1] and the unfolded neutrino spectrum obtained from that data set [8] suggest that the data sample is strongly dominated by atmospheric neutrinos. If this holds, a difference of the significance distribution to that of randomized data sets, which follows a Gaussian (see above), would indicate that our assumption of a flat background in right ascension is not correct. Also in this case, the observed significance distribution follows our expectation. The significance distribution for both tests is shown in Fig. 11.

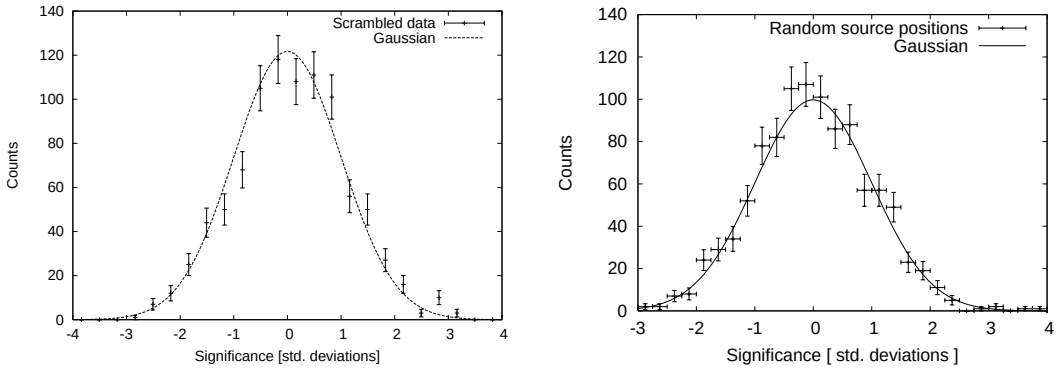

(a) (b)

Fig. 11. Significance distribution for selected sources in scrambled data sets (a) and for samples of 10 sources with random source positions evaluated with the unscrambled data set (b).

No statistically significant signal was found, in this limited data sample, above pure background; only upper limits could be derived. To calculate these limits we used Feldman-Cousins [63] confidence intervals and Poisson statistics. Systematic errors, estimated to be at the $\pm 30\%$ level, were not taken into account. The measured event rates, the background expectation and the resulting upper limits in terms of event counts and integral neutrino fluxes above 10 GeV are presented in Table 3 and visualized in Figure 12. A dedicated analysis of systematics for a multi-year dataset is currently in preparation. For most of the declination range, the sensitivity (90% C.L.) of the point source analysis for the considered data set is about $2 \cdot 10^{-8}\mathrm{cm}^{-2}\ \mathrm{s}^{-1}$ [1]. A comparison with the limit per source obtained from stacking (see Table 3) shows the progress reached by the source stacking method.

7 Summary

We have performed a systematic classification of AGN. This is the basis of a source stacking analysis of TeV neutrinos with the AMANDA neutrino telescope. Neutrinos are assumed to be produced in optically thick jets or accretion disks. The optical depths of these sites and consequently the average energy of photons leaving the source are unknown. We therefore select the sources according to the photon flux at different energies. Most of the available photon data were not collected at the same time as the considered AMANDA data set. Thus, the time variability of AGN was not considered in this analysis.

sample	N_{src}	N_ν^{obs}	N_ν^{bg}	n_{lim}	f_{lim}	f_{lim}/N_{src}
IR blazars	11	7	10.17	3.0	2.0	0.18
keV blazars (ROSAT)	8	4	6.68	2.4	1.6	0.2
keV blazars (HEAO-A)	3	2	2.47	3.5	2.8	0.9
GeV blazars	8	6	5.3	6.3	4.0	0.5
unid. GeV sources	22	15	14.9	7.6	5.6	0.25
TEV blazars	5	4	4.53	4.1	2.8	0.56
GPS and CSS	8	7	6.14	6.4	4.3	0.54
FR-I galaxies	1	0	0.56	1.9	1.3	1.3
FR-I without M87	20	9	11.50	3.9	2.7	0.14
FR-II galaxies	17	10	13.42	3.7	2.7	0.16
radio-weak quasars	11	4	7.55	1.9	1.3	0.12

Table 3
Results for the year 2000 data: Number of sources N_{src}, measured number of events N_ν^{obs}, the corresponding background N_ν^{bg} and the 90% C.L. limits on the event counts (n_{lim}) and on the integral flux for an E^{-2} spectrum above 10 GeV (f_{lim}) in units of $10^{-8}\mathrm{cm}^{-2}\ \mathrm{s}^{-1}$. f_{lim}/N_{src} represents the limit per source.

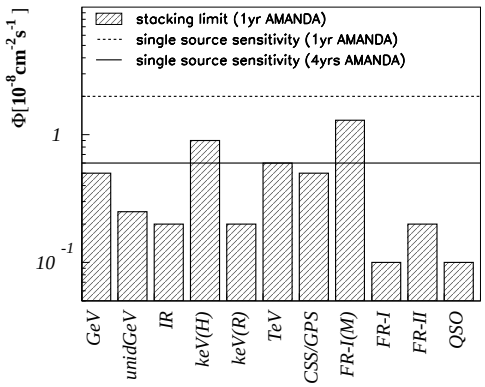

Fig. 12. Limits on the neutrino flux from an average source in the generic AGN classes using data from the year 2000. The average sensitivity to single point sources is indicated by horizontal lines for this data set [1] a well as for a 4 year data set [3].

With the hypothesis that the TeV neutrino flux is proportional to the corresponding photon flux, we have optimized the number of sources to be included.

For most source classes, an optimum of $8-12$ sources to be stacked has been found. For these, the source stacking analysis is more sensitive than the point

source analysis of a single source. Exceptions have been found for FR-I and FR-II radio galaxies. While FR-I galaxies are dominated by the single source M87, there are too many FR-II galaxies with a similar flux in order to converge at a reasonably small number of sources to be stacked.

For the data of the year 2000, no significant deviation from the background expectation was found. In a next step, the stacking method will be applied to several years of AMANDA data. Optimizing the method to an angular resolution of less than 1° and better background rejection, it will be adapted to the 1 km^3 IceCube array [57]. Starting with the selection of southern sky sources, it is also applicable to other neutrino telescopes [58,59,60,61,62].

A The distance correction of fluxes

The distance dependence of a measured flux F_ν at the observer's frequency ν of a source with luminosity $L_{\nu'}$ is given by

$$F_\nu \mathrm{d}\nu = L_{\nu'} \frac{1}{4\pi d_l(z)^2} \mathrm{d}\nu' \,, \tag{A.1}$$

with the luminosity distance d_l and the frequency at the source $\nu' = \nu(1+z)$. The luminosity distance as a function of redshift is given by

$$d_l(z) = \begin{cases} \frac{(1+z)c}{H_0 \cdot |\Omega_k|^{0.5}} \sin\left\{ |\Omega_k|^{0.5} \cdot I(z) \right\} \,, & \text{if } \Omega_k < 0 \,, \\ \frac{(1+z)c}{H_0} \,, & \text{if } \Omega_k = 0 \,, \\ \frac{(1+z)c}{H_0 \cdot |\Omega_k|^{0.5}} \sinh\left\{ |\Omega_k|^{0.5} \cdot I(z) \right\} \,, & \text{if } \Omega_k > 0 \,, \end{cases} \tag{A.2}$$

see [64]. $I(z)$ is given by

$$I(z) = \int_0^z \left[(1+z')^2 \cdot (1 + \Omega_m z') - \Omega_\Lambda z'(2+z') \right]^{-0.5} dz' \,, \tag{A.3}$$

with the normalized curvature Ω_k. We used $\Omega_m = 0.27$, $\Omega_\Lambda = 0.75$ according to [65] and $h = 0.71$ according to [66].

For a power law spectrum with spectral index α, the redshift results in

$$L_{v'} \mathrm{d}\nu' = L_{\nu \cdot (1+z)} \cdot (z+1)^{\alpha+1} \mathrm{d}\nu \,. \tag{A.4}$$

Finally, the correction to $z = 0.1$ for a source at redshift z is given by

$$F^{z=0.1} = F \cdot \left(\frac{d_l(z)}{d_l(z=0.1)} \right)^2 \cdot \left(\frac{z+1}{0.1+1} \right)^{\alpha+1} \,. \tag{A.5}$$

B Source catalogs for AMANDA

radio source (1950 coord)	**IR source** (1950 coord)	F_{5GHz} [Jy]	**SI**	$F_{12\mu\mathrm{m}}$ [Jy]	$F_{25\mu\mathrm{m}}$ [Jy]	$F_{60\mu\mathrm{m}}$ [Jy]	$F_{100\mu\mathrm{m}}$ [Jy]	**z**	$F_{5GHz}^{z=0.1}$ [Jy]
1Jy 0851+20	IRAS F08519+2017	2.62	0.11	0.2838	0.4335	0.8911	1.1580	0.306	36.8
1Jy 1404+28	IRAS F14047+2841	2.95	0.80	0.1850	0.3994	0.7288	0.9376	0.077	1.7
1Jy 1641+39	IRAS F16413+3954	10.81	0.54	0.1068	0.2918	0.5999	1.3840	0.594	756
1Jy 1308+32	IRAS F13080+3237	1.53	0.20	0.1744	0.2710	0.4198	0.5760	0.996	525
1Jy 2200+42	IRAS F22006+4202	4.77	-0.13	0.1393	0.2495	0.4029	1.9690	0.070	2.2
1Jy 1732+38	IRAS F17326+3859	1.13	0.85	0.0964	0.1688	0.3280	0.6699	0.970	246
1Jy 1803+78	IRAS F18036+7827	2.62	0.25	0.0931	0.1826	0.3083	0.7386	0.684	301
1Jy 0735+17	IRAS F07352+1749	1.99	0.05	0.1868	0.1907	0.2519	0.5198	0.424	66.3
1Jy 0716+71	IRAS F07162+7126	1.12	0.22	0.1121	0.1260	0.2374	0.7825	0.300	15.7
1Jy 0235+16	IRAS F02358+1623	2.85	1.03	0.1105	0.1068	0.2344	0.9074	0.851	403
1Jy 1418+54	IRAS F14180+5437	1.09	0.38	0.0659	0.0857	0.2121	0.5459	0.151	2.7

Table B.1
Strongest IR sources in blazar catalog. F_{5GHz} stands for the radio flux at 5 GHz, while the mean IR flux at $12, 25, 60$ and 100 μm is labeled $F_{12\mu m} \ldots F_{100\mu m}$. SI is the spectral index α determined between 2.7 GHz and 5 GHz. z is the cosmological redshift. The distance corrected radio flux flux is given by $F_{5GHz}^{z=0.1}$. The IR data has been taken in the 1980s.

X-ray source (2000 coord)	**Radio source** (1950 coord)	F_X [cnt/s]	**HR I**	**HR II**	F_{5GHz} [Jy]	**SI**	**z**	$F_{5GHz}^{z=0.1}$
1RXS J172320.5+341756	S4 1721+343	1.0160	0.20	0.07	0.934	-0.43	0.206	5.2
1RXS J225358.0+160855	1Jy 2251+158	0.6094	0.96	0.26	17.42	0.64	0.859	3100
1RXS J084125.1+705342	1Jy 0836+710	0.5308	0.62	0.19	2.59	-0.32	2.16	15300
1RXS J115324.4+493108	1Jy 1150+497	0.3699	0.26	0.07	1.12	-0.48	0.334	22.1
1RXS J164258.9+394822	1Jy 1641+399	0.3253	-0.18	-0.05	10.81	0.54	0.594	756
1RXS J192748.0+735757	1Jy 1928+738	0.2772	0.86	0.25	3.34	-0.01	0.36	73.1
1RXS J220315.6+314535	1Jy 2201+315	0.2424	0.94	0.28	2.32	0.24	0.298	29.9
1RXS J092702.8+390221	1Jy 0923+392	0.2376	-0.16	0.38	8.73	1.03	0.698	756
1RXS J072153.2+712031	1Jy 0716+714	0.1925	0.12	0.19	1.12	0.22	0.30	14.7
1RXS J163813.1+572028	1Jy 1637+574	0.1158	0.03	0.24	1.42	0.35	0.750	202
1RXS J074541.2+314249	S2 0742+31	0.1147	0.81	0.57	0.96	-0.23	0.462	43.6
1RXS J220244.4+421626	1Jy 2200+420	0.1144	0.98	0.44	4.77	-0.13	0.070	2.2
1RXS J083454.3+553417	1Jy 0831+557	0.1027	0.58	0.03	5.65	-0.46	0.242	39.7
1RXS J135703.6+191915	1Jy 1354+195	0.1005	0.42	0.69	1.56	-0.07	0.720	239

Table B.2
ROSAT sources identified with strong radio blazars. The mean X-ray flux as measured by ROSAT in 1990/1991 (6 month of observation time) is given by F_X. The hardness ratios HR I and HR II display the ratio between low and high energy X-rays: HR $= (n_{HE} - n_{LE})/(n_{HE} + n_{LE})$. For HR I the low energy range is $0.1 - 0.4$ keV and the high energy range is $0.5 - 2.0$ keV. For HR II the intervals are $0.5 - 0.9$ keV and $0.9 - 2.0$ keV. SI is the spectral index α determined between 2.7 GHz and 5 GHz. F_{5GHz} stands for the radio flux at 5 GHz. SI is the spectral index α determined between 2.7 GHz and 5 GHz with $F_v \propto v^{\alpha}$. The distance corrected radio flux flux is given by $F_{5GHz}^{z=0.1}$.

HEAO-A source (1950 coord)	**radio source** (1950 coord)	F_X [cnt/s]	F_{5Ghz} [Jy]	**SI**	**z**	$F_{5GHz}^{z=0.1}$ [Jy]
1H0717+714	1Jy 0716+714	0.0030	1.12	0.22	0.30	14.7
1H1154+294	S3 1156+29	0.0029	0.89	-0.44	0.73	167
1H1922+746	1Jy 1928+73	0.0027	3.34	-0.01	0.36	73.1

Table B.3
HEAO-A sources identified with strong radio blazars: The mean flux measured by HEAO-A is given by F_X, and F_{5GHz} stands for the radio flux at 5 GHz. All data have been taken within an 6 month interval in 1977-1978, though the observation times of individual sources are shorter. SI is the spectral index α determined between 2.7 GHz and 5 GHz with $F_v \propto v^{\alpha}$. The cosmological redshift is given by z and the distance corrected radio flux flux is given by $F_{5GHz}^{z=0.1}$.

GeV source (2000 coord)	**radio source** (1950 coord)	$\mathbf{F}_{5\mathrm{GHz}}$ [Jy]	**SI**	$\mathbf{F}_{\mathrm{GeV}}^{\mathrm{max}} * 10^{-8}$ $[s^{-1}cm^{-2}]$	$\mathbf{F}_{\mathrm{GeV}}^{\mathrm{mean}} * 10^{-8}$ $[s^{-1}cm^{-2}]$	**z**
3EG J0450+1105	1Jy 0446+112	1.23	0.56	109.5	14.9	1.207
3EG J1635+3813	1Jy 1633+382	4.02	0.73	107.5	58.4	1.814
3EG J0530+1323	1Jy 0528+134	3.97	0.47	93.5	93.5	2.060
3EG J0237+1635	1Jy 0235+164	2.85	1.03	65.1	25.9	0.940
3EG J2254+1601	1Jy 2251+158	17.42	0.64	53.7	53.7	0.859
3EG J1200+2847	S3 1156+29	0.89	-0.44	50.9	7.5	0.73
3EG J2202+4217	1Jy 2200+420	4.77	-0.13	39.9	11.1	0.069
3EG J1608+1055	1Jy 1606+106	1.49	0.42	34.9	25.0	1.226
3EG J1614+3424	1Jy 1611+343	2.67	0.10	26.5	26.5	1.401
3EG J0829+2413	S3 0827+24	0.94	0.05	24.9	24.9	2.05
3EG J0204+1458	1Jy 0202+149	2.47	-0.43	23.6	8.7	0.405
3EG J2232+1147	1Jy 2230+114	3.61	-0.50	19.2	19.2	1.037
3EG J1738+5203	1Jy 1739+522	1.98	0.68	18.2	18.2	1.375
3EG J0721+7120	1Jy 0716+714	1.12	0.22	17.8	17.8	0.300
3EG J0737+1721	1Jy 0735+178	1.99	0.05	16.4	16.4	0.424
3EG J0958+6533	1Jy 0954+658	1.46	0.35	15.4	6.0	0.368
3EG J2358+4604	1Jy 2351+456	1.42	-0.05	14.3	14.3	1.992
3EG J0239+2815	1Jy 0234+285	1.44	-0.24	13.8	13.8	1.21
3EG J0917+4427	S4 0917+449	0.80	0.66	13.8	13.8	2.18
3EG J0853+1941	1Jy 0851+202	2.62	0.11	10.6	10.6	0.306
3EG J0845+7049	1Jy 0836+710	2.59	-0.32	10.2	10.2	2.172
3EG J0952+5501	1Jy 0954+556	2.28	-0.19	9.1	9.1	0.901

Table B.4
3EG sources identified with strong radio blazars: F_{5GHz} is the radio flux at 5 GHz, SI is the spectral index α determined between 2.7 GHz and 5 GHz. The maximum and the mean flux as measured by EGRET in 1991-1995 are listed under $\mathrm{F}_{\mathrm{GeV}}^{\mathrm{max}}$ resp. $\mathrm{F}_{\mathrm{GeV}}^{\mathrm{mean}}$. z is the cosmological redshift. The EGRET catalog uses the reference system of the yea 2000.

EGRET source	F_{GeV}^{max} $[10^{-8}s^{-1}cm^{-2}]$	F_{GeV}^{mean} $[10^{-8}s^{-1}cm^{-2}]$	$\|b\|$ [°]	3EG Id. flag
3EG J2243+1509	73.1	9.9	37.49	
3EG J2255+1943	62.2	5.8	35.43	a
3EG J1835+5918	60.6	60.6	25.07	
3EG J1212+2304	50.8	3.3	80.32	
3EG J1850+5903	46.7	12.6	23.18	
3EG J0439+1555	42.9	4.8	19.98	
3EG J0010+7309	42.3	42.3	10.54	
3EG J1822+1641	40.6	7.1	13.84	
3EG J2314+4426	40.4	13.9	15.10	
3EG J2352+3752	37.5	6.1	23.54	a
3EG J1825+2854	34.3	6.5	18.03	
3EG J0407+1710	32.1	7.3	25.06	
3EG J1824+3441	28.7	8.1	20.14	
3EG J1308+8744	23.9	7.6	29.38	
3EG J1733+6017	22.9	8.7	32.94	
3EG J1227+4302	21.7	4.6	73.33	
3EG J1347+2932	21.0	9.6	77.50	
3EG J0910+6556	18.3	5.9	38.56	
3EG J1323+2200	18.1	5.2	81.15	a
3EG J0215+1123	18.0	9.3	46.37	
3EG J0329+2149	17.2	7.4	27.88	
3EG J0245+1758	16.9	8.8	37.11	
3EG J0426+1333	14.0	14.0	23.82	
3EG J0917+4427	13.8	13.8	44.19	a
3EG J2248+1745	12.9	12.9	36.17	

Table B.5
Unidentified and weakly identified extragalactic EGRET sources, possibly blazars. SI is the spectral index α determined between 2.7 GHz and 5 GHz. F_{5GHz} is the radio flux at 5 GHz, SI is the spectral index α determined between 2.7 GHz and 5 GHz. The maximum and the mean flux as measured by EGRET in 1991-1995 are listed under $\mathrm{F}_{\mathrm{GeV}}^{\mathrm{max}}$ resp. $\mathrm{F}_{\mathrm{GeV}}^{\mathrm{mean}}$.

X-ray source	**other name**	F_{TeV} [crab flux]	**5 GHz flux** [Jy]	**z**
1ES 1101+38.4	Mrk 421	0.04-7.4	0.72	0.0300
1ES 1652+39.8	Mrk 501	0.33-6	1.38	0.0336
H 1426+428	-	0.03-0.08	0.04	0.1290
1ES 1959+650	-	0.05-2.20	0.25	0.0470
1ES 2344+514	-	0.03	0.23	0.0440

Table B.6
TeV blazars with $\delta > 10°$, The TeV fluxes are listed in units of the flux of the Crab nebula, $dJ_\gamma/dE = (2.79 \pm 0.02 \pm 0.5) \cdot 10^{-7}(E/TeV)^{-2.59\pm0.03\pm0.05}$. F_{5GHz} stands for the radio flux at 5 GHz, while the cosmological redshift is given by z.

Coordinate name (1950 coord)	**other name**	**Sample**	**Mag**	**z**	F_{5GHz} [Jy]	θ [arcsec]	ν_m [MHz]	$\log P_{5GHz}$	**Size** [kpc]
0248+430	n. a.	G	15.5	1.316	1.24	0.06	5000	27.9	0.474
0134+329	3C 48	C	16.1	0.367	5.3	0.50	80	27.3	2.255
0738+313	n. a.	G	16.1	0.630	3.62	0.010	5300	27.6	0.061
1458+718	3C 309.1	C	16.8	0.905	3.5	2.11	40	28.0	14.831
1345+125	4C 12.50	G	17.0	0.122	3.05	0.080	400	26.0	0.160
1328+307	3C 286	C	17.2	0.849	7.4	3.2	80	28.2	21.966
0740+380	3C 186	C	17.6	1.063	0.3	2.2	40	27.2	16.330
1328+254	3C 287	C	17.7	1.055	3.2	0.048	50	28.1	0.355
0538+498	3C 147	C	17.8	0.545	8.2	0.55	150	27.9	3.101
1442+101	OQ 172	CG	17.8	3.535	1.20	0.02	900	29.3	0.185
0221+276	3C 67	C	18.0	0.309	0.9	2.5	50	26.3	10.100
2352+495	n. a.	G	18.4	0.237	1.49	0.050	700	26.3	0.168
2249+185	3C 454	C	18.5	1.758	0.8	0.66	40	28.1	5.562
0518+165	3C 138	C	18.8	0.760	4.1	0.60	100	27.8	3.942
0345+337	3C 93.1	C	19.0	0.244	0.8	0.25	60	26.0	0.858
1153+317	4C 31.38	C	19.0	1.557	1.0	0.9	100	28.0	7.397
1203+645	3C 268.3	C	19.0	0.371	1.1	1.36	80	26.6	6.175
1323+321	4C 32.44	CG	19.0	0.369	2.39	0.06	500	26.9	0.272
1443+77	3C 303.1	C	19.0	0.267	0.5	1.7	100	26.0	6.219
1819+39	4C 39.56	C	19.0	0.4	1.0	0.44	100	26.6	2.091
1358+624	4C 62.22	CG	19.9	0.429	1.80	0.07	500	26.9	0.347
0127+233	3C 43	C	20.0	1.459	1.1	2.60	20	28.0	21.054
0428+205	OF 247	CG	20.0	0.219	2.38	0.250	1100	26.4	0.793
1117+146	4C 14.41	G	20.0	0.362	1.00	0.08	500	26.5	0.358
1829+29	4C 29.56	C	20.0	0.842	1.1	3.1	100	27.3	21.212

Table B.7
GPS and CSS sources fulfilling our selection rules. In Sample, G means GPS and C means CSS. Mag is the optical magnitude. The cosmological redshift is given by z, while F_{5GHz} stands for the radio flux at 5 GHz. θ is the angular size of the source. ν_m is the turnover frequency and P_{5GHz} stands for log of power at 5 GHz (assuming isotropic emission). The linear size of the sources is listed in kpc. The data were compiled from previous catalogs in 1998.

Source	F_{178MHz} [Jy]	**SI**	δ [°]	**RA** [°]	**z**
3C 274.0	1050.	-0.76	12.6667	12.4667	0.004
3C 84.0	61.3	-0.78	41.3167	3.26667	0.017
3C 433.0	56.2	-0.75	24.85	21.35	0.101
3C 310.0	55.1	-0.92	26.2	15.0333	0.054
3C 338.0	46.9	-1.19	39.65	16.4333	0.029
3C 465.0	37.8	-0.75	26.75	23.5833	0.029
3C 83.1	26.0	-0.64	41.6667	3.23333	0.025
3C 264.0	26.0	-0.75	19.8833	11.7	0.020
3C 66.0	24.6	-0.62	42.75	2.33333	0.021
3C 386.0	23.9	-0.59	17.15	18.6	0.017
3C 272.1	19.4	-0.60	13.15	12.3667	0.003
3C 288.0	18.9	-0.85	39.1	13.6	0.246
3C 315.0	17.8	-0.72	26.3	15.1833	0.108
3C 31.0	16.8	-0.57	32.1333	1.06667	0.016
3C 28.0	16.3	-1.06	26.1333	0.883333	0.195
3C 442.0	16.1	-0.96	13.5833	22.2	0.026
3C 305.0	15.7	-0.85	63.4667	14.8	0.041
3C 231.0	14.6	-0.28	69.9167	9.85	0.000
3C 296.0	13.0	-0.67	11.0333	14.2333	0.023
3C 293.0	12.7	-0.45	31.6833	13.8333	0.045
3C 76.1	12.2	-0.77	16.2333	3	0.032
3C 449.0	11.5	-0.58	39.1	22.4833	0.017
3C 346.0	10.9	-0.52	17.35	16.6833	0.161
3C 314.1	10.6	-0.95	70.95	15.1667	0.119

Table B.8
FR-I radio galaxies: F_{178MHz} is the mean radio flux at 178 MHz, SI is the spectral index α determined between 178 MHz and 750 MHz, RA and δ stand for right ascension and declination, respectively in the reference system of 1950. All data were collected before 1985. Note, in the original 3CRR catalog, the spectral index is defined with an opposite sign. The cosmological redshift is given by z.

Source	F_{178MHz} [Jy]	**SI**	δ [°]	**RA** [°]	**z**
3C 123.0	189.0	-0.70	29.5667	4.55	0.218
3C 295.0	83.5	-0.63	52.4333	14.15	0.461
3C 196.0	68.2	-0.79	48.3667	8.15	0.871
3C 452.0	54.4	-0.78	39.4167	22.72	0.081
3C 33.0	54.4	-0.76	13.0667	1.1	0.059
3C 390.3	47.5	-0.75	79.7167	18.75	0.056
3C 98.0	47.2	-0.78	10.2833	3.93	0.030
3C 438.0	44.7	-0.88	37.7667	21.88	0.290
3C 20.0	42.9	-0.67	51.7833	0.67	0.174
3C 219.0	41.2	-0.81	45.85	9.28	0.174
3C 234.0	31.4	-0.86	29.0167	9.97	0.184
3C 61.1	31.2	-0.77	86.0833	2.17	0.186
3C 79.0	30.5	-0.92	16.9	3.12	0.255
3C 330.0	27.8	-0.71	66.0667	16.15	0.550
3C 427.1	26.6	-0.97	76.35	21.07	0.572
3C 47.0	26.4	-0.98	20.7	1.55	0.425
3C 388.0	24.6	-0.70	45.5	18.7	0.090
3C 280.0	23.7	-0.81	47.6	12.9	0.997
3C 228.0	21.8	-1.00	14.5667	9.78	0.552
3C 109.0	21.6	-0.85	11.0667	4.17	0.305
3C 55.0	21.5	-1.04	28.6167	1.9	0.734
3C 268.1	21.4	-0.59	73.2833	11.95	0.973
3C 225.0B	21.3	-0.94	13.9833	9.65	0.582
3C 192.0	21.1	-0.79	24.3	8.03	0.059
3C 401.0	20.9	-0.71	60.5667	19.65	0.201

Table B.9
FR-II radio galaxies: F_{178MHz} is the mean radio flux at 178 MHz, SI is the spectral index α determined between 178 MHz and 750 MHz RA and δ stand for right ascension and declination, respectvely in the reference system of 1950. All data were collected before 1985. Note, in the original 3CRR catalog, the spectral index is defined with an opposite sign. The cosmological redshift is given by z.

quasar name	$F_{60\mu m}$ [mJy]	z	$\log \nu f_{14.5}$
PG 0050+124	2293	0.061	-13.30
PG 1351+640	757	0.087	-13.86
PG 1440+356	652	0.077	-13.70
PG 1613+658	635	0.129	-13.97
PG 1119+120	546	0.049	-13.82
PG 1501+106	486	0.036	-13.54
PG 1700+518	480	0.292	-13.90
PG 1351+236	364	0.055	-13.75
PG 1543+489	348	0.400	-14.52
PG 2214+139	337	0.067	-13.70
PG 1634+706	318	1.334	-14.00
PG 1402+261	229	0.164	-14.10
PG 1248+401	224	1.030	-14.59
PG 0947+396	201	0.206	-14.57
PG 1148+549	196	0.969	-14.30
PG 1114+445	191	0.144	-14.14
PG 0804+761	191	0.100	-13.70
PG 0838+770	174	0.131	-14.25
PG 0906+484	172	0.118	-14.30
PG 1229+204	163	0.064	-13.74
PG 0844+349	163	0.064	-13.82
PG 1411+442	162	0.089	-13.87
PG 1448+273	117	0.065	-13.81
PG 1444+407	117	0.267	-14.28
PG 1415+451	112	0.114	-14.05
PG 0052+251	93	0.155	-14.09

Table B.10
Radio-weak quasars from the BQS sorted according to IRAS mean flux at $\lambda = 60\mu$m, $F_{60\mu m}$. The cosmological redshift is given by z. The logarithm of the energy flux density at $10^{14.5}$ is given by $\log \nu f_{14.5}$. For the BQS, data were taken until 1983, IRAS data have been taken in the 1980s.

Radio source	**other name**	**Samples (Position)**
1Jy 0316+41	NGC 1275	IR blazars (1), keV blazars (ROSAT (1) and HEAO-A (1))
1Jy 1652+398	Mrk 501	keV blazars (ROSAT (2) and HEAO-A (2))
1Jy 1222+13	M 84	IR blazars (6)
1Jy 0055+30	NGC 315	IR blazars (11)
1Jy 1807+698		keV blazars (HEAO-A (31))

Table B.11
Nearby intrinsically weak sources. Due to their proximity they nevertheless may contribute significantly to the neutrino flux. We propose to analyze them as individual sources.

References

[1] J. Ahrens et al., Physical Review Letters 92 (2004) 070201.

[2] M. Ackermann et al., Physical Review D 71 (2005) 077102.

[3] M. Ackermann et al., Proceedings of the 29th ICRC, 2005, astro-ph/0509330.

[4] A. Cillis, R. Hartman and D. Bertsch, Astrophysical Journal 601 (2004) 142.

[5] A. Cillis, D. Torres and O. Reimer, Astrophysical Journal (2005).

[6] C.M. Urry and P. Padovani, The Publications of the Astronomical Society of the Pacific 107 (1995) 803.

[7] http://amanda.uci.edu.

[8] K. Münich et al., Proceedings of the 29th ICRC, 2005, astro-ph/0509330.

[9] C.P. O'Dea, The Publications of the Astronomical Society of the Pacific 110 (1998) 493.

[10] M. Blazejowski et al., Astrophysical Journal 630 (2005) 130.

[11] R. Antonucci and J. Miller, Astrophysical Journal 297 (1985) 621.

[12] M. O'Dowd, C.M. Urry and R. Scarpa, Astrophysical Journal 580 (2002) 96.

[13] H. Falcke and P.L. Biermann, Astronomy & Astrophysics 293 (1995) 665.

[14] H. Falcke, W. Sherwood and A. Patnai, Astrophysical Journal 471 (1996) 106.

[15] M. Cappi et al., Advances in Space Research 25 (2000) 815.

[16] C.P. O'Dea and S.A. Baum, Astronomical Journal 113 (1997) 148.

[17] B.L. Fanaroff and J.M. Riley, Monthly Notices of the Royal Astronomical Society 167 (1974) 31.

[18] H. Falcke, M.A. Malkan and P.L. Biermann, Astronomy & Astrophysics 298 (1995) 375.

[19] H. Falcke, . Gopal-Krishna and P.L. Biermann, Astronomy & Astrophysics 298 (1995) 395.

[20] K. Mannheim, Proceedings of the XXXIInd Rencontres de Moriond, "Very High Energy Phenomena in the Universe", Les Arcs, France, p. 17, 1997.

[21] T.C. Weekes, ArXiv Astrophysics e-prints (2003), astro-ph/0312179, Planary talk held at the 28th Int. Cosmic Ray Conf.

[22] R.C. Hartman et al., Astrophysical Journal Suppl. Ser. 123 (1998) 79.

[23] P.L. Biermann and P.A. Strittmatter, Astrophysical Journal 322 (1987) 643.

[24] F.W. Stecker et al., Physical Review Letters 66 (1991) 2697.

[25] L. Nellen, K. Mannheim and P. Biermann, Physical Review D (1993) 5270.

[26] F.W. Stecker and M.H. Salamon, Space Sci.Rev. 75 (1996) 341.

[27] J.G. Learned and K. Mannheim, Annu. Rev. Nucl. Part. Sci. 50 (2000) 679.

[28] A. Bell, Monthly Notices of the Royal Astronomical Society 182 (1978) 147.

[29] A. Bell, Monthly Notices of the Royal Astronomical Society 182 (1978) 443.

[30] R.J. Protheroe, Towards the millenium in Astrophysics, Problems and Prospects. Proceedings of International School of Cosmic Ray Astrophysics 10th Course, p. 3.

[31] K. Mannheim, R.J. Protheroe and J.P. Rachen, Physical Review D 63 (2001) 023003.

[32] H. Krawczynsk et al., Astrophysical Journal 601 (2004) 151.

[33] W. Cui et al., High Energy Gamma-Ray Astronomy: 2nd International Symposium, AIP Conference Proceedings, edited by F. Aharonian, H. Völk and D. Horns Vol. 745, pp. 455–461, 2005.

[34] A. Mücke and R.J. Protheroe, Astroparticle Physics 15 (2001) 121.

[35] A. Mücke and R.J. Protheroe, Proc. 27th Int. Cosmic Ray Conf. p. 1153, 2001.

[36] J.K. Becker, P.L. Biermann and W. Rhode, Astroparticle Physics 23 (2005) 355.

[37] H. Kühr et al., Astronomy and Astrophysics Supplement 45 (1981) 367.

[38] H. Kühr et al., MPIfR Preprint 55 (1979/1981).

[39] M. Moshir et al., Bulletin of the American Astronomical Society 22 (1990) 1325.

[40] K.S. Wood et al., Astrophys.J.Suppl. Ser. 56 (1984) 507.

[41] W. Voges et al., Astronomy & Astrophysics 349 (1999) 389.

[42] http://cossc.gsfc.nasa.gov/.

[43] D. Sowards-Emmerd, R.W. Romani and P.F. Michelson, Astrophysical Journal 590 (2003) 109.

[44] H. Gehrels et al., Nature 404 (2000) 363.

[45] R. Fanti et al., Astronomy & Astrophysics 231 (1990) 333.

[46] C. Stanghellini et al., Astronomy and Astrophysics Supplement 131 (1998) 303.

[47] H. Spinrad et al., The Publications of the Astronomical Society of the Pacific 97 (1985) 932.

[48] R. Laing et al., Monthly Notices of the Royal Astronomical Society 204 (1983) 151.

[49] M. Schmidt and R.F. Green, Astrophysical Journal 269 (1983) 352.

[50] D. Sanders et al., Astrophysical Journal 347 (1989) 29.

[51] K. Woschnagg et al., Proceedings of the XXIst International Conference on Neutrino Physics and Astrophysics, Paris, 2004, Nuclear Physics B (Proc. Suppl.) 143 (2005).

[52] J. Ahrens et al., Physical Review Letters 90 (2003) 251101.

[53] F. Aharonian et al., Astronomy & Astrophysics 403 (2003) L1.

[54] M. Beilicke et al., Proceedings of the 29th ICRC, 2005

[55] R. Protheroe, A.C. Donea and A. Reimer, Astroparticle Physics 19 (2003) 559.

[56] D.E. Alexandreas et al., Nuclear Instruments & Methods A 328 (1993) 570.

[57] J. Ahrens et al., Astroparticle Physics 20 (2004) 507.

[58] http://baikalweb.jinr.ru.

[59] ANTARES collaboration, astro-ph/9707136, see also http://antares.in2p3.fr.

[60] htpp://www.nestor.rg.gr.

[61] http://nemoweb.lns.infn.it.

[62] http://www.km3net.org.

[63] G.J. Feldman and R.D. Cousins, Physical Review D 57 (1998) 3873.

[64] S.M. Carroll, W.H. Press and E. L.Turner, Ann. Rev. Astron. Astrophys. 30 (1992) 499.

[65] D.N. Spergel et al., Astrophysical Journal Suppl. 148 (2003) 175.

[66] A. Balbi et al., Astrophysical Journal Letters 588 (2003) L5.